*The following manuscript is non-peer reviewed preprint and is under consideration for publication in Boundary Layer Meteorology.*

# Approaching coherent turbulence and the roll-cell transition with Lagrangian coherent structures and objective fluxes

**Nikolas Aksamit[1,2] • Marwan Katurji[2] • Jiawei Zhang[3]**

Received: DD Month YEAR/ Accepted: DD Month YEAR/ Published online: DD Month YEAR


**Abstract**

We present the first analysis of objective and material vortices in Large Eddy Simulations of atmospheric boundary layer turbulence. We extract rotating fluid features that maintain structural coherence over time for near-neutral, transitional, and convective boundary layers. In contrast to traditional analysis of coherent structures in turbulent boundary layers, we provide the first objective (frame-indifferent) identification of temporally coherent vortex boundaries that are responsible for organizing tracer distributions. We compare these rotating structures with qualitative descriptions of horizontal rolls and convective cells arising from decades of observational studies. We also quantify their contribution to turbulent fluxes of heat under varying atmospheric stability. Using recently developed tools from the theory of objective transport barriers, we derive connections between the relative orthogonality of objective momentum and heat transport with the presence of rolls and cells. This suggests the relationship between momentum and heat transport through vortex surfaces may help explain the physics behind roll-cell transitions.

**Keywords** Heat Flux • Lagrangian Coherent Structures • Large Eddy Simulation • Stability Analysis • Vortex Identification

---

✉ Nikolas Aksamit
nikolas.aksamit@uit.no

[1] Department of Mathematics and Statistics, UiT - The Arctic University of Norway, Tromso, 9037, Norway

[2] marwan.katurji@canterbury.ac.nz School of Earth and Environment, University of Canterbury, Christchurch, 8041, New Zealand

[3] Jiawei.Zhang@scionresearch.com Scion, New Zealand Forest Research Institute, Rotorua 3010, New Zealand

## 1 Introduction

Various geometries of fluid-organizing structures in atmospheric turbulence are evident at scales from millimetres to thousands of kilometres. Such features can be seen in swirls of smoke rising off a match head, the patterning of cloud streets in the atmospheric boundary layer, and synoptic scale cyclones in the troposphere. In the atmospheric boundary layer (the first 2km above ground level), convection results in the development of two prevalent structures - the horizontal convective roll and the convective cell (Moeng and Sullivan 1994; Svensson et al. 2017; Yagi et al. 2017; Jayaraman and Brasseur 2021). In weakly convective and neutral boundary layers, significant horizontal shear outweighs convective forcing, causing horizontal rolls to dominate the flow as quasi-streamwise vortices (Young et al. 2002). In a highly convective (unstable) boundary layer, open convective cells dominate the flow, similar to Rayleigh-Bénard convection, with updrafts around the boundaries of polygonal cells, and downdrafts in the center (Moeng and Sullivan 1994; Salesky et al. 2017). The physical mechanisms driving the transition from rolls to convective cells are poorly understood, especially in intermediate atmospheric stability regimes when the relative role of both mechanical and buoyancy forces is important (Salesky et al. 2017; Jayaraman and Brasseur 2021).

This transition is of fundamental interest in fluid dynamics as the physical fluid transport mechanisms are changing. For boundary layer meteorology, the two structures have different impacts on turbulent transport, with rolls generating more efficient turbulent momentum transport than cells (Salesky et al. 2017). The transience and quasi-coherence of these different features also contribute to mean flux values that inhibit surface energy balance closure (Foken et al. 2011; Mauder et al. 2020). Furthermore, understanding heat and momentum transport during this transition is critical for turbulence resolving numerical weather prediction tools such as Large Eddy Simulation (LES) models, as the performance of subgrid scale parameterizations still need to be assessed (Schalkwijk et al. 2015; Lehner and Rotach 2018).

Previous observational and numerical investigations have studied the presence and the development of horizontal convective rolls and polygonal convective cells under varying surface heat flux conditions (Deardorff 1972; LeMone 1973, 1976; Grossman 1982; Weckwerth et al. 1997, 1999; Khanna and Brasseur 1998; Park and Baik 2014). Salesky et al. 2017) performed the first systematic LES study on the transition of rolls to cells. Their work analyzed 14 large-eddy simulations ranging from neutral to highly convective boundary layers through relative eddy flux contributions (e.g., quadrant analysis), mean vertical profiles, and the statistical symmetries of the vertical velocity field. While certain turbulent flux behaviour was ascribed to roll or cells, this statistical analysis fell short of calculating any fluxes corresponding to individual structures as they did not delimit the actual surfaces of these three-dimensional vortices. Over a smaller range of stabilities, (Jayaraman and Brasseur 2021) also performed a detailed LES study of convective influence on horizontal rolls from a statistical standpoint, but again lacked analysis of the actual geometric structures.

To study the behaviour and impact of rolls and cells, being able to accurately identify their boundaries in a given flow is of fundamental interest as our understanding of these features originates from visual evidence of tracers (water vapor) that have been organized by fluid structures in the atmosphere. Some the earliest systematic evidence of rolls and cells was made possible with airborne imagery and satellite remote sensing (e.g., Christian and Wakimoto 1989; Young et al. 2002). Thus, it is intuitive to study these structures from the geometric fluid structure perspective, if possible. This approach, however, contrasts with the common approach of seeking evidence of structures through their statistical imprints on profiles or velocity distributions.

To accurately identify and study the atmospheric structures that organize tracer distributions in the ways we have classically observed, we need to utilize structure identification diagnostics that define features that are experimentally observable. By this we mean coherent structure diagnostics which are used to evaluate the existence and behaviour of fluid structures should define the same observable structures highlighted by passive tracers. Developing structure identification diagnostics that maintain experimental verifiability has not been of great concern to the boundary layer meteorology community, but it is something that one needs to consider when developing structure identification methods. This disconnect is evident if one compares standard boundary layer diagnostics that identify coherent structures with what is required to describe material deformation of a fluid as follows.

The organization of passive tracers in any fluid (e.g., heat, trace gases, or water vapor), whether in cloud streets, streaks, or convective plumes is the result of the material deformation of the fluid. After several decades of debate, it was widely accepted as a fundamental axiom of continuum mechanics that material deformation of any fluid is indifferent to the position of the observer, and thus indifferent to Euclidean frame changes (Gurtin 1981). That is, to identify an influential coherent structure in the atmosphere, our identification methods need to be indifferent to any changes in reference frame of the form

$$\boldsymbol{y}(t) = \boldsymbol{Q}(t)\boldsymbol{x}(t) + \boldsymbol{b}(t)$$

where $\boldsymbol{x}(t)$ and $\boldsymbol{y}(t)$ are position vectors in a given reference frame, $\boldsymbol{Q}(t)$ is a time-varying three-dimensional rotation, and $\boldsymbol{b}(t)$ is a time-varying translation. For example, the same cloud geometry will appear in photographs whether they are taken from a tripod in a field, a moving car, or from a circling airplane. In this way, one can also see that the dimensions and structure of our material features of interest should also be indifferent to the reference frame. A frame-indifferent scalar value transforms as $P(x) = \tilde{P}(y)$, and a frame-indifferent vector transforms as $\tilde{v} = Qv$ (Truesdell and Noll 2004). Frame-indifference is often referred to as *objectivity* and any material flow feature diagnostic should satisfy this benchmark (Drouot 1976; Drouot and Lucius 1976; Astarita 1979; Lugt 1979).

Conceptual models of hairpin vortices, rolls, thermal plumes, and cells describe material fluid features and are ubiquitous in the meso- and micro-meteorology literature. There has been limited connection, however, between numerically-simulated vortices and those experimentally observed in the laboratory or atmosphere. One cause for this may stem from the lack of objectivity of the common tools for coherent structure identification. Wind velocity, components of Reynolds decompositions, and products of fluctuating velocity components (e.g., Reynolds stress, turbulence kinetic energy, quadrant analysis products) are known to not actually be experimentally-observable and thus cannot describe material behaviour, or fluid-deforming structures (Speziale 1998; Kaszás et al. 2023). On the other hand, measurements of atmospheric state parameters such as temperature, pressure, and humidity are frame indifferent scalars, and can provide clues to the presence of structures in meteorological station measurements.

The study and understanding of heat and momentum transport for process-based analyses in the atmospheric boundary layer has been strongly influenced by the spatial and temporal scale of data that has been classically available. Temporally-resolved point measurements of wind and scalars from meteorological towers facilitate statistical studies of fluxes of heat and momentum that harness some temporal averaging with Reynolds decomposition and eddy-covariance or with flux-profile methods (Foken 2008). There is no doubt that we have a significantly better understanding of ABL turbulence thanks to the idea of turbulent fluxes, and non-objective coherent structure identification methods, such as quadrant analysis. Our goal here is to introduce the advantages of a complementary way of studying fluid behaviour that is rigorously linked to the material behaviour of fluid, instead of statistical signatures arising from the presence of those structures.

For spatially resolved velocity fields, the most used vortex identification methods employ diagnostic scalar fields, such as the Q-, $\lambda_2$-, Δ- and $\lambda_{ci}$-parameters (Hunt et al. 1988; Jeong and Hussain 1995; Zhou et al. 1999; Adrian et al. 2000; Gao et al. 2011). Iso-surfaces of Q, $\lambda_2$, $\Delta$ and $\lambda_{ci}$ are not frame-indifferent and hence the structures they define cannot predict observed material tracer patterns (Haller 2005, 2020). As mentioned before, this lack of self-consistency means such structures may be correlated with measured scalar concentrations or turbulent fluxes (e.g., Westerweel et al. 2009; Eisma et al. 2021), but there can be no causal description of an observable fluid structure. Several modifications of these vortex diagnostics can make them objective (e.g., Liu et al. 2019a, b), but as there is a missing connection to material mixing and transport, identifying the right vortex is strongly dependent on the user. The subjectivity associated with user-defined values for these non-objective diagnostics was recently highlighted by Dong and Tian (2020).

We describe rolls and cells as frame-indifferent, material, and rotationally coherent Lagrangian structures for nearly neutral, transitional, and highly convective boundary layers. This work provides the first objective description of cells and rolls in Large Eddy

Simulations of the ABL. We first verify that the features we define do indeed resemble qualitative descriptions of rolls and cells in section 3.1. In section 3.2, we discuss the role these rotationally coherent structures play in the advective and turbulent transport of heat when compared with the surrounding incoherent turbulent atmosphere. Lastly, we compare objective heat and momentum transport for varying atmospheric stability, and draw a connection between structure formation, mechanical and thermal influences, and alignment of diffusive fluxes.

# 2 Methods

## 2.1 Rotationally Coherent Lagrangian Coherent Structures

Lagrangian coherent structures (LCS) behave as the hidden skeleton of fluid flow (Peacock and Haller 2013). Acting as the finite time analogue of invariant manifolds from the mathematical field of time-dependent dynamical systems, LCSs have been mathematically derived as the most influential transport barriers that exhibit specific characteristics (Haller 2023). For any arbitrary material surface in an unsteady fluid (i.e., a two-dimensional surface consisting of infinitesimal fluid particles that deforms with the flow), advective transport across that surface will be zero because the surface deforms under advection, by definition. As such, there are infinitely many material barriers to advective transport. LCS are material surfaces that maintain structural coherence over a finite time interval with exceptional behaviour, such as being maximally repelling or attracting surfaces (hyperbolic LCS), or local maximizers of shear among material surface that maintain rotational coherence (elliptic LCS).

LCS have proven beneficial for furthering our understanding of coherent atmospheric structures and transport barriers, but this is still a nascent field of research (see e.g., Tallapragada et al. 2011; Olascoaga et al. 2012; Rutherford et al. 2012; BozorgMagham and Ross 2015; Wang et al. 2017). Specific examples include studies on zonal jets (Beron-Vera et al. 2012), atmospheric rivers (Garaboa-Paz et al. 2015), and the polar vortex (Serra et al. 2017). Of particular relevance to the ABL are the studies identifying LCS in laboratory boundary layers using two-dimensional Particle Image Velocimetry (Green et al. 2007; Pan et al. 2009; Wilson et al. 2013; He et al. 2016; Eisma et al. 2021), predicting downdraft and significant shear events in near-surface doppler lidar measurements at the Hong Kong International Airport (Tang et al. 2011; Knutson et al. 2015), studying atmospheric Karman Vortex street from satellite wind measurements (Günther et al. 2021), and understanding aerosol dispersion patterns in the stratosphere (Aksamit et al. 2021). The above research all relied on two-dimensional projections of velocity fields to describe inherently three-dimensional phenomena. Only recently have studies of elliptic LCS and objective momentum and heat transport barriers been successfully conducted in fully three-dimensional turbulent experimental and numerical flows (Neamtu-Halic et al. 2019; Aksamit and Haller 2022; Aksamit et al. 2023).

To study rolls and cells in ABLs of varying stability, we utilized time-resolved three-dimensional velocity fields to identify candidate vortices as regions of strong fluid coherence and material rotation. Specifically, in a given velocity field $\boldsymbol{v}(\boldsymbol{x},t)$, fluid particle trajectories $\boldsymbol{x}(t;\ t_0,\boldsymbol{x}_0)$ originating at some initial position $\boldsymbol{x}_0$ at time $t_0$ are generated by the differential equation

$$\dot{\boldsymbol{x}} = \boldsymbol{v}(\boldsymbol{x},t).$$

These trajectories define the flow map $\boldsymbol{F}_{t_0,t}(\boldsymbol{x}_0) = \boldsymbol{x}(t;\ t_0,\boldsymbol{x}_0)$, which is the unique function that maps fluid particle positions from their initial position and time, to their position at some time $t$, according to the velocity field $\boldsymbol{v}(\boldsymbol{x},t)$. To detect elliptic LCSs over a time window $[t_0,t_1]$, we utilize the *Lagrangian-Averaged Vorticity Deviation* (*LAVD*) (Haller et al. 2016). This is defined as the mean of the magnitude of the difference of the pointwise vorticity $\omega = \nabla \times \boldsymbol{v}$ along a trajectory from the spatial mean of vorticity at each time step. Formally, to obtain the time $t_0$ location of elliptic LCSs, we calculate

$$\mathrm{LAVD}_{t_0}^{t}(\boldsymbol{x}_0) = \frac{1}{|t_1 - t_0|}\int_{t_0}^{t} |\boldsymbol{\omega}(\boldsymbol{x}(s;\boldsymbol{x}_0), s) - \overline{\boldsymbol{\omega}}(s)|ds$$

where the overbar indicates a spatial mean. This quantity is objective for a given fluid volume of interest, but exact values depend on how that domain is defined. For our experiments, we consistently use the entire spatial domain of our LES.

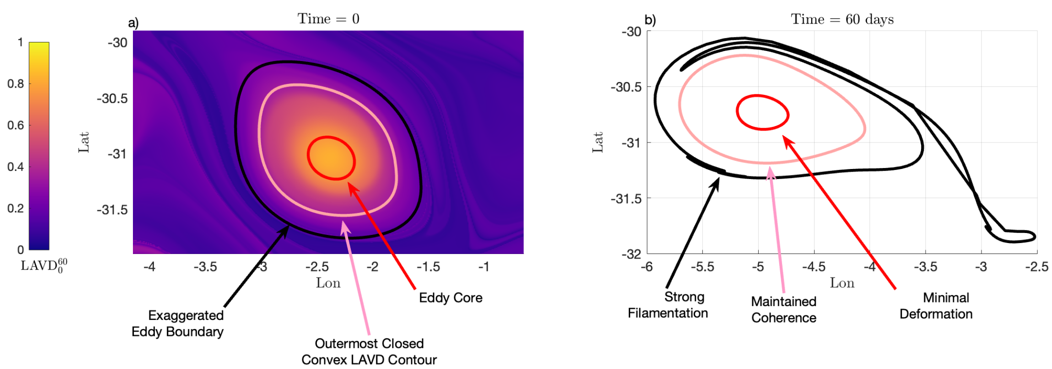


**Fig 1**: Example of time evolution of fluid particles surrounding an elliptic LCS (red) in a 2D ocean flow over 60 days

In recent years, *LAVD* has been used as a diagnostic to identify the boundaries of coherent oceanic eddies and vortices (Abernathey and Haller 2018; Beron-Vera et al. 2019) and quantify the transport of fluid inside these coherent structures over pan-oceanic distances. In Figure 1, we illustrate the dynamic behaviour of an *LAVD*-identified ocean surface current eddy in the Agulhas Rings region as computed from geostrophic ocean surface currents that are freely available from the Copernicus Environment Monitoring Service (CMEMS, 2019). The *LAVD* field was computed over 60 days of fluid advection, and the boundary of the materially coherent eddy at time $t = 0$ is identified in pink as the outermost closed convex *LAVD* contour surrounding a local *LAVD* maximum (Figure 1a). In Figure 1a, we also include a level-set contour corresponding to a higher *LAVD* value in the eddy core in red, and a spatially magnified version of the pink eddy boundary in black. This magnified contour is thus outside the boundary of what we predict is a materially coherent eddy. In Figure 1b, we plot the final position of the fluid particles corresponding to each contour after 60 days of advection. As an appropriately chosen elliptic LCS, both the pink boundary and the central core remain minimally deformed though they have undergone significant rotation and the eddy center has traveled nearly 250 km through open ocean. As it was originally drawn outside of the material eddy boundary, the outermost black contour exhibits significant filamentation after 60 days.

We can extend this analysis to three-dimensional flows where locations of elliptic LCSs can be identified as smooth cylindrical *LAVD* level-surfaces that surround a one-dimensional *LAVD* ridge (Neamtu-Halic et al. 2019). In the present work we rely on the relaxed coherent Lagrangian vortex criteria utilized by Aksamit et al. (2023) in rotating Rayleigh-Bénard convection by not seeking a central *LAVD* ridge or enforcing a cylindrical shape. Neglecting these requirements comes with a computational advantage, while still capturing material rotational features. In fact, Aksamit et al. (2023) showed that any arbitrary *LAVD* level-surface exhibits exceptional momentum and heat transport blocking behaviour orthogonal to its surface, even though the calculation of *LAVD* does not consider these fields. Furthermore, the ability of arbitrary *LAVD* surfaces to organize the transport of momentum and heat was largely independent of the length of the integration time $[t_0, t_1]$, with shorter intervals resulting in better flux limiting behaviour.

### 2.2 Objective and non-objective Fluxes

For a scalar concentration $c$ that satisfies the classic advection-diffusion equation with diffusivity $\kappa > 0$, the instantaneous diffusive transport through an evolving material surface $M(t)$ is an objective quantity that can be written as

$$\Sigma(t, M) = \int_{M(t)} \kappa \nabla c \cdot \boldsymbol{n} \, dA \tag{1}$$

with $\boldsymbol{n}(\boldsymbol{x}, t)$ being a smooth unit normal vector field along $M(t)$. In contrast to the convective scalar flux through the surface, $\boldsymbol{v}c \cdot \boldsymbol{n}$, diffusive scalar transport through a surface in eq (1) does not change with varying reference frames and can be thought of as a physical property intrinsic to the surface and the flow. This idea is of particular relevance to micrometeorology where a given flow may be characterized by choosing $M$ to be a fixed (non-material) horizontal plane, and then calculating the vertical convective scalar flux at that height at each time (Stull, 1988). This vertical convective scalar flux is not actually a frame-indifferent quantity, and therefore not an intrinsic quantity of the flow as it depends on the user.

Similarly, the convective transport of momentum, $\rho\boldsymbol{v}(\boldsymbol{v}\cdot\boldsymbol{n})$, varies between reference frames and is an insufficient benchmark to quantify the momentum transport through a given surface in a given flow. To circumvent this problem, Haller *et al.* (2020) introduced the instantaneous diffusive transport of linear momentum $\boldsymbol{f}(\boldsymbol{x},t) = \rho\boldsymbol{v}(\boldsymbol{x},t)$ through $M(t)$,

$$\psi(t,M) = \int_{M(t)} \nu\rho\nabla^2\boldsymbol{v}\cdot\boldsymbol{n}dA \tag{2}$$

The integrands of equations (1) and (2) thus provide objective vector fields for quantifying the magnitude and alignment of diffusive heat and momentum transport for arbitrary surfaces in a flow. This frame-indifferent and individual feature-focused approach to quantifying heat and momentum flux has helped explain the relative influences of Coriolis and convective forces on specific vortices in direct numerical simulations of rotating Rayleigh-Bénard flow (Aksamit et al. 2023). We apply a similar approach to suggest a spatially and temporally resolved objective diagnostic that predicts the dominance of rolls and cells and is based on the underlying physics of heat and momentum transport.

In turbulent boundary layers, distinguished flow features that advect heat (plumes, vortices, etc.) appear as structures with limited mixing with the surrounding fluid. The boundaries of such features, across which the mixing of heat is limited, can be identified by locally maximal temperature gradients. That is, they are surfaces across which diffusive transport is maximized, meaning the temperature gradient is normal to these surfaces. In contrast, Lagrangian coherent structures have been correlated with diffusive momentum transport barriers that constrain the distributions of momentum (Haller et al. 2020; Aksamit et al. 2023). The surfaces of these structures are then tangent to the objective momentum transport vector field.

Given this theoretical difference in flux vector orientation, Aksamit et al. (2023) used the inner product of diffusive heat and momentum flux vector fields to quantify the relative agreement of momentum and heat transport barriers in rotating Rayleigh-Bénard convection. The more closely aligned that instantaneous barriers of heat and momentum are, the closer to zero the inner products of objective heat and momentum flux vectors on those surfaces are. In their work, the distribution of momentum and heat flux vector alignments helped explain the varying roles of Coriolis enhanced and convection dominated structures in organizing the flow. We seek to extend these findings to ABLs where heat and momentum alignment can in turn be used to diagnose the presence of cells and rolls, and describe transitional behaviour, in an objective way.

*2.2.1 Non-objectivity of turbulent momentum and heat flux*

In this section, we highlight a fundamental difference between our approach, and traditional turbulent flux-based flow diagnostics. The behaviour of turbulent flows is often characterized by Reynolds decomposition and the Reynolds stress tensor, which is frame-indifferent (objective) only if one removes the same average values from every point of the flow field (Speziale 1979). When quantifying turbulent fluxes at a chosen height or through a chosen surface, researchers typically rely on instantaneous or time-averaged turbulence covariances (e.g., $w'\theta'$ or $u'w'$). In contrast to the full Reynolds stress tensor, $w'\theta'$ and $u'w'$ are actually not frame-indifferent, and thus cannot describe material behaviour of the flow. That is, these values cannot predict experimentally observable structures that organize tracers, such as rolls and cells. This can be seen in the following way.

Decompose the velocity field into a mean and fluctuating part

$$v(x,t) = \overline{v} + \boldsymbol{v}'(x,t)$$

where averaging must be performed over ensembles of experiments with the same initial and boundary conditions, indexed by α:

$\overline{v} = \frac{1}{N}\sum_{\alpha=1}^{N} v^{\alpha}$.

Recall, Euclidean frame-changes, or physical changes of an observer's reference frame can be written as

$$\boldsymbol{y}(t) = \mathbf{Q}(t)\boldsymbol{x}(t) + \boldsymbol{b}(t)$$

where $x$ and $y$ are positions, $\mathbf{Q}(t)$ is a three-dimensional rotation, and $\boldsymbol{b}(t)$ is a translation vector. By differentiating the frame-change with respect to time, we observe the transformation of velocity vectors between frames as,

$$\tilde{\boldsymbol{v}} = \dot{\mathbf{Q}}(t)\boldsymbol{x}(t) + \mathbf{Q}(t)\boldsymbol{v}(t) + \dot{\boldsymbol{b}}(t)$$

We can then write a fluctuating velocity vector in the new frame as

$$\widetilde{\boldsymbol{v}'} = \dot{\mathbf{Q}}(t)\boldsymbol{x}(t) + \mathbf{Q}(t)\boldsymbol{v}(\boldsymbol{t}) + \dot{\boldsymbol{b}}(t) - \frac{1}{N}\sum_{\alpha=1}^{N} \dot{\mathbf{Q}}(t)\boldsymbol{x}(t) + \mathbf{Q}(t)\boldsymbol{v}^{\boldsymbol{\alpha}} + \dot{\boldsymbol{b}}(t)$$

As we are averaging over an ensemble of experiments that undergo the same time-varying frame change, we can simplify this equation by moving terms with no dependence on α outside the summation, resulting in the following form

$$\widetilde{\boldsymbol{v}'} = \dot{\mathbf{Q}}(t)\boldsymbol{x}(t) + \mathbf{Q}(t)\boldsymbol{v}(\boldsymbol{t}) + \dot{\boldsymbol{b}}(t) - \dot{\mathbf{Q}}(t)\boldsymbol{x}(t) - \dot{\boldsymbol{b}}(t) - \mathbf{Q}(t)\left[\frac{1}{N}\sum_{\alpha=1}^{N} \boldsymbol{v}^{\boldsymbol{\alpha}}\right]$$

$$= \mathbf{Q}(t)[\boldsymbol{v}(\boldsymbol{t}) - \overline{\boldsymbol{v}}].$$

This is precisely the form necessary for fluctuating velocity vectors to be frame indifferent when a Reynolds decomposition is performed with ensemble averages.

Researchers often invoke the ergodic hypothesis that ensemble and temporal averages are equivalent. That is, for large enough N and M, $\frac{1}{N}\sum_{\alpha=1}^{N} \boldsymbol{v}^{\boldsymbol{\alpha}}(x,t) = \frac{1}{M}\sum_{i=1}^{M} v(x,t_i)$. While this may be true, $\mathbf{Q}$ and $\boldsymbol{b}$ are also time dependent, and we are left with

$$\widetilde{\boldsymbol{v}'} = \dot{\mathbf{Q}}(t)\boldsymbol{x}(t) + \mathbf{Q}(t)\boldsymbol{v}(\boldsymbol{t}) + \dot{\boldsymbol{b}}(t) - \frac{1}{M}\sum_{i=1}^{M} \dot{\mathbf{Q}}(t_i)\boldsymbol{x}(t_i) + \mathbf{Q}(t_i)\boldsymbol{v}(\boldsymbol{x}(\boldsymbol{t_i}),\boldsymbol{t_i}) + \dot{\boldsymbol{b}}(t_i)$$

which does not simplify as above. Spatial averaging creates similar issues as the fluctuating velocity would transform as

$$\widetilde{\boldsymbol{v}'} = \dot{\mathbf{Q}}(t)\boldsymbol{x}(t) + \mathbf{Q}(t)\boldsymbol{v}(\boldsymbol{t}) + \dot{\boldsymbol{b}}(t) - \frac{1}{M}\sum_{i=1}^{k} \dot{\mathbf{Q}}(t)\boldsymbol{x_i} + \mathbf{Q}(t)\boldsymbol{v}(\boldsymbol{x_i},\boldsymbol{t}) + \dot{\boldsymbol{b}}(t)$$

Furthermore, the individual components of the fluctuating velocity vector, and individual terms in the Reynolds stress tensor are not frame indifferent scalar values, even for ensemble averaging. This can be seen term by term by writing $\mathbf{Q} = [q_{ij}]$ and $\widetilde{\boldsymbol{v}'_i} = q_{\boldsymbol{i1}}\boldsymbol{v}'_{\boldsymbol{1}} + q_{i2}\boldsymbol{v}'_{\boldsymbol{2}} + q_{i3}\boldsymbol{v}'_{\boldsymbol{3}}$. Then, $\widetilde{\boldsymbol{v}'_i} = \boldsymbol{v}'_i$ only for $\mathbf{Q}$ being the identity matrix, not for any rigid-body rotation, so the fluctuating velocity component values $\boldsymbol{v}'_i$ are not frame indifferent. As temperature is a frame indifferent scalar, this implies $\boldsymbol{v}'_i\boldsymbol{\theta}'$ and $\overline{\boldsymbol{v}'_i\boldsymbol{\theta}'}$ are also frame dependent for each component $i$. Furthermore, one can expand

$$\widetilde{\boldsymbol{v}'_i\boldsymbol{v}'_j} = (q_{\boldsymbol{i1}}\boldsymbol{v}'_{\boldsymbol{1}} + q_{i2}\boldsymbol{v}'_{\boldsymbol{2}} + q_{i3}\boldsymbol{v}'_{\boldsymbol{3}})(q_{\boldsymbol{j1}}\boldsymbol{v}'_{\boldsymbol{1}} + q_{j2}\boldsymbol{v}'_{\boldsymbol{2}} + q_{j3}\boldsymbol{v}'_{\boldsymbol{3}}),$$

and conclude individual terms of instantaneous and time-averaged Reynolds stress are also not objective.

This lack of objectivity has wide implications for studies that attempt to identify turbulent coherent structures through quadrant analysis and contours of $u'w'$ (for a review of this approach, see Wallace 2016)). From the fundamental axioms of continuum mechanics, no such structure will ever have a causal relationship with fluid deformation. As we will also discuss in the Results, structures identified using Reynolds stress and turbulent heat flux level-sets are not even reliably correlated with fluid deformation. This issue is further complicated in mildly complex terrain where buoyancy and shear forces become non-orthogonal and there is no a-priori known temporal scale for averaging (Serafin et al. 2018).

### 2.3 Large Eddy Simulations

Observational and numerical studies indicate that $-z_i/L$ is well correlated with the dominance of rolls and cells, with small values associated with roll and large values associated with cells. The transitional values are more disputed, but previous LES studies suggest that the transition from rolls to cells begins around $15 < -z_i/L < 25$ for flat, horizontally homogeneous terrain (Deardorff 1972; Khanna and Brasseur 1998; Salesky et al. 2017). Initial investigations suggested $-\frac{z_i}{L} = 25$ to be too small for our simulations, and we settled on a slightly larger value where transitional behaviour became more pronounced. Accordingly, we compare objective fluxes of momentum and heat across Lagrangian coherent structures for three ABL simulations $-\frac{z_i}{L} \in \{6.7, 29.2, 589.2\}$. For each stability regime, the PALM (Parallelized Atmospheric Large eddy simulation Model) model (Maronga et al. 2020) using incompressible Navier-Stokes equation with Boussinesq approximation is used in this work to generate boundary layer simulation data. The turbulence recycling method is used to reduce the computational cost in the main simulations (Maronga et al. 2020). To do so, for each of the three main simulations, the model first used a pre-cursor simulation to prepare the turbulence inflow data for the main simulation. Detailed pre-cursor run configurations can be found in Table 1a. The pre-cursor simulations run long enough to make sure that the turbulent flow field has reached quasi-equilibrium. The turbulent flow field from the pre-cursor runs were then used in the respective main simulations as the upwind turbulence inflow in the main simulation domain. Two nested domains were used in all the main simulations to resolve finer turbulence structures (Table 1b). For each stability regime, we calculate *LAVD* in volumes of 500 m, 2500 m, 125 m corresponding to the streamwise, spanwise, and vertical dimensions.

Table 1a. Configuration for the precursor run simulations

| | Domain size (x,y,z) (km) | Grid resolution (x,y,z) (m) | Simulation time |
|---|---|---|---|
| Near neutral | 12.3x12.3x6.9 | 64x64x54 | 24h |
| Transitioning | | | 24h |
| Convective | | | 4h |

Table 1b. LES Configuration

| | Domain size (x,y,z) (km) | Grid resolution (x,y,z) (m) | Simulation time | $z_i$ | \|L\| | $-z_i/L$ |
|---|---|---|---|---|---|---|
| Near neutral | D01: 24.5x24.5x6.9 D02: 8.2x8.2x3.5 D03: 6.1x6.1x2.3 | D01: 64x64x54 D02: 32x32x18 D03: 16x16x9 | 1.5h (Only the last hour was used in the analysis.) | 2268 | 336.1 | 6.7 |
| Transitioning | | | | 3713 | 127.1 | 29.2 |
| Convective | | | | 2345 | 3.98 | 589.2 |

# 3 Results

## 3.1 Describing Vertical Fluid Motion with Frame Dependent Structures

To help motivate our Lagrangian coherent structure approach, we start with a simple example from the near-neutral ABL simulation. As shown in section 2.2.1, components of fluctuating velocity vectors and Reynolds stress components are not frame-indifferent, and cannot describe the material fluid structures responsible for coherent motions. There may still, however, be correlations between the location of coherent fluid motions and their imprint on these diagnostic fields. We investigate these potential correlations in a simple test of describing vertical motion of fluid near the surface of a near-neutral boundary layer.

Quadrant analysis is a common Eulerian turbulent coherent structure diagnostic, that focuses on the fluctuating values of streamwise and vertical windspeed

$$u' = u - \bar{u},\ w' = w - \bar{w},$$

and isolates large magnitude Reynolds stress ($u'w'$) events (Lu and Willmarth 1973). These events are then separated into quadrants depending on the sign of the fluctuating components $u'$ and $w'$, with quadrants two and four, termed ejections and sweeps, contributing disproportionately to the total Reynolds stress.

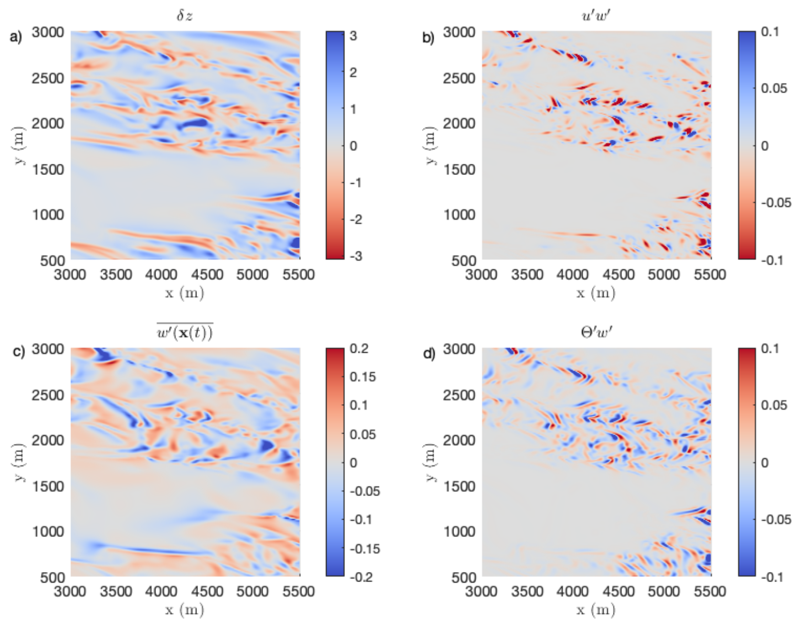


**Fig 2:** Comparison of the 10-second vertical change of fluid particle position (a), kinetic momentum flux (b), Lagrangian-averaged vertical velocity fluctuations (c), and kinetic heat flux (d) in a near-neutral atmospheric boundary layer at z = 5 metres

In turbulent boundary layers, ejections and sweeps are often used to describe near-surface signatures of the bursting-cycle, a theoretical process of coherent fluid moving away from the surface and the in-rush of turbulent fluid to replace it (Kline et al. 1967; Wallace 2016). In Figure 2 we present streamwise-spanwise planes at 5 metres above the surface in a near-neutral boundary layer. In Figure 2a, we present the 10 second vertical displacement of fluid by initializing a $1500 \times 1500$ grid of fluid particles at $z = 5$ metres, and advecting them backwards in time from $t_0$ to $t_0 - 10s$. The resulting contour plot in Fig 2a shows the vertical height change for fluid particles with blue shading indicating fluid dropping from an initially higher position, and red corresponding with fluid rising from a lower position in forward time. We then compare this material fluid deformation to the instantaneous $t_0$ fields of $u'w'$, and $\Theta'w'$ in Figures 2b and 2d, calculated from ten second averaging over the plane of observation.

There is some qualitative agreement between regions of large vertical change in fluid trajectories with the largest magnitudes of $u'w'$ and $\Theta'w'$, suggesting larger turbulent fluxes may occur during significant vertical transport of fluid. It is immediately clear, however, that there is no direct connection between the magnitude, or sign, of values in 2b or 2d with what the fluid was doing immediately prior to $t_0$. Even at short time scales, $u'w'$ and $\Theta'w'$ cannot determine if nearby air is rising or falling.

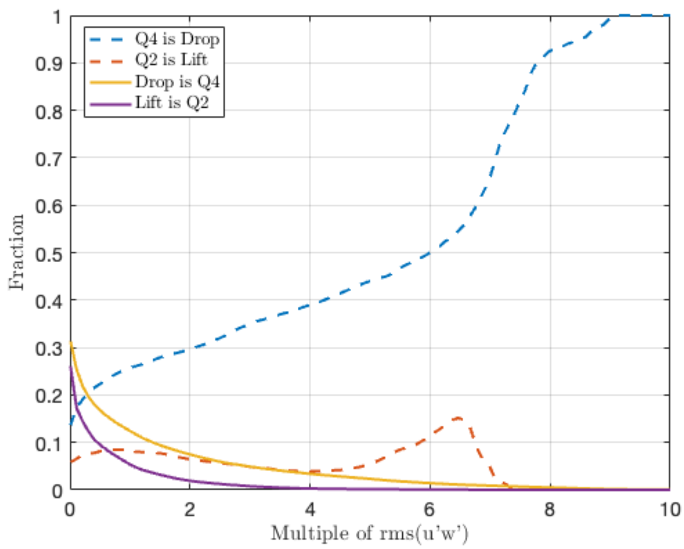


**Fig 3:** Connection between quadrant analysis designated events of varying threshold and the actual vertical motion of fluid particles from Figure 2

For an additional comparison, we also perform a Reynolds decomposition for each grid cell in our flow spanning the ten seconds of fluid advection, as one would do if sampling at separate meteorological stations throughout the domain. Though this results in a non-physical reference frame change, it gives the greatest advantage for vertical velocity fluctuations to accurately describe relative motion of nearby fluid. We then average $w'$ along the same 10-second trajectories used in 2a, to see if descending or ascending fluid consistently experience the same fluctuating value on its path. Contours of this diagnostic in Figure 2c show qualitatively more similar features to the actual fluid elevation change, such as more elongated features in the streamwise direction, but there is still not a direct match. In fact there are many examples of large positive Lagrangian-averaged $w'$ in 2c that corresponds with descending fluid in 2a.

We quantify these qualitative descriptions of turbulent fluctuations and vertical fluid motion in Figure 3. We refer to any fluid that descends by more than 1 metre in the ten seconds prior to $t_0$ as a true drop, and all fluid particles that ascend by more than 1 metre as a true lift. This is a liberal description of significant vertical fluid motion, as can be seen from the distribution of $\delta z$ in Figure 2a.

When performing quadrant analysis, the user must choose a Reynolds stress magnitude threshold (“quadrant hole”) above which quadrant 2 and quadrant 4 features are defined as ejections, or sweeps, respectively. There is a wide range of values available in the literature, so we instead investigate all thresholds between 0.001 and 10 times the root mean square of $|u'w'|$. The fraction of instantaneous sweeps that correspond with true drops varies from 15% to 100% at a hole size of nine times the r.m.s.. For the majority of hole sizes, less than 50% of sweeps corresponded with fluid that is actually descending significantly. Ejections were less successful at identifying rising fluid as less than 20% of ejections actually corresponded with lifting fluid.

In Figure 3, we also show the fraction of drops and lifts that could be identified as sweeps or ejections. For the smallest Reynold stress threshold, sweeps were maximally effective at diagnosing descending fluid with approximately 30% of drops identified. Ejections nearly matched this accuracy, but more quickly decreased in accuracy as quadrant hole size increased.

This simple example shows the disconnect between an intuitive interpretation of fluctuating velocity terms, a very common method of coherent structure identification, and the true fluid behaviour. It is through this seeming dissonance that we differentiate our research from other approaches. Rather than looking at coherence in turbulent velocity fields or time series to suggest the presence of an atmospheric structure or behaviour, we define coherence with respect to the material deformation of the fluid, and use those structures to investigate the role of rolls and cells. With the actual fluid surfaces in hand, we can determine their influence on turbulent heat fluxes, and better understand the physics of their origin.

**3.2 LAVD in the atmospheric boundary layer**

We calculated *LAVD* over ten second windows spanning sixty minutes of simulated boundary layer flow. For computational economy, we randomly selected 10 second intervals in each minute of the sixty-minute datasets. A ten second integration interval was empirically chosen to balance the computational expense of Lagrangian particle tracking with feature resolution. Integration times from two to sixty seconds were also investigated. As with previous *LAVD* studies of heat transport barriers, structure geometry and flux barrier behaviour was found to be robust over a wide range of integration times. We show an example of this in the appendix.

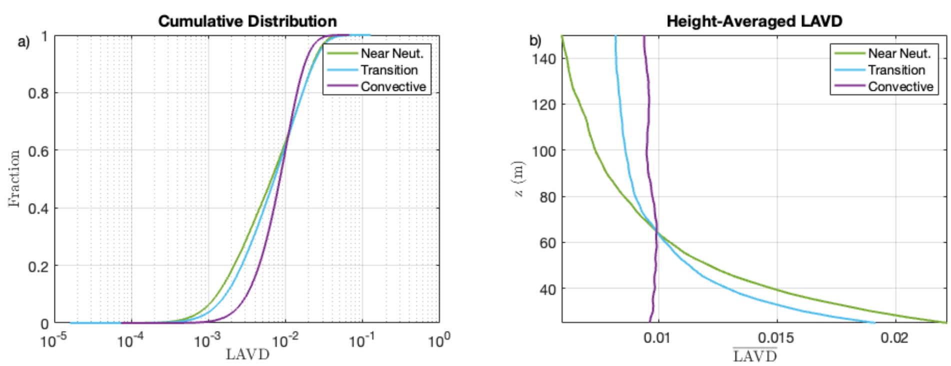


**Fig 4:** Empirical cumulative distributions of LAVD and height-averaged values of LAVD for the three stability simulations

Some general properties of the transition from shear-dominated to convection-dominated flows can be seen in bulk flow behaviour described in Figure 4. Figure 4a shows empirical cumulative distribution functions (CDF) of *LAVD* for the three cases, and Figure 4b shows height-averaged values of *LAVD*. In the near-neutral case, the surface-shear dominance is clear as highly rotational fluid is concentrated near the surface, with the largest mean *LAVD* values below 60 metres out of the three experiments. The CDF reveals that more fluid undergoes minimal rotation and is not part of a coherent vortex in the near-neutral case than in the transitional or convective case. That is, strong rotation in the fluid is isolated to relatively rare, but strong near-surface vortices.

For the strongly convective case, we see that convective mixing results in a much more uniform distribution of $LAVD$ values across all heights. The relatively smaller influence of shear no longer restricts the formation of coherent Lagrangian vortices to the near surface region, though a slight decrease in average $LAVD$ is evident above 65 metres. The CDF of $LAVD$ shows a shift away from extreme values, and is more concentrated around a mean value of $10^{-2}$. The transitional case reveals more rotational structures between 65 and 150 metres above the surface than the near-neutral simulation, but lower average $LAVD$ in the near surface region. This exists as an intermediate step between the convective and neutral regimes. These profiles also reveal a relative enhancement of upper level mixing possible with the onset of convection, and a complimentary dampening of roll-formation that decreases near-surface fluid rotation begins as temperature gradients increase.

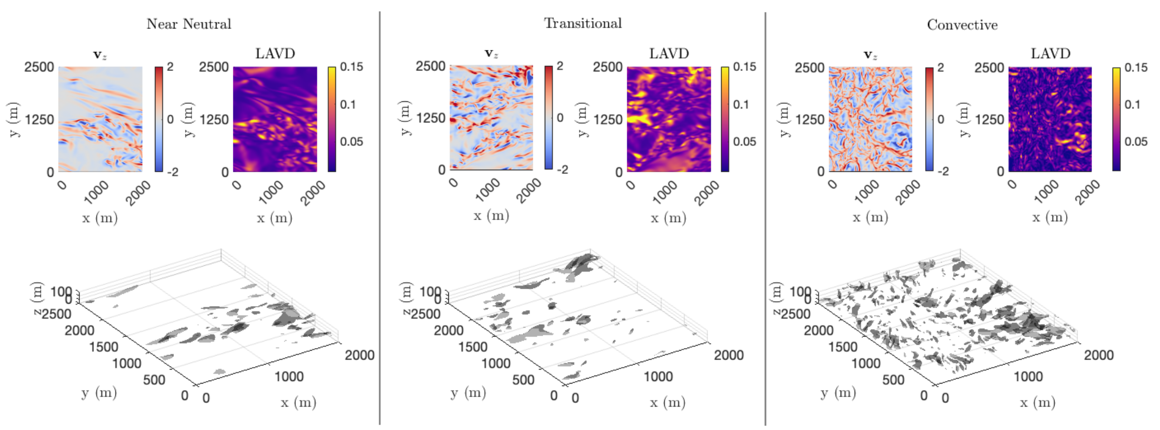


**Fig 5:** Comparison of vertical velocity and LAVD on $z = 25\,m$ streamwise-spanwise planes, as well as LAVD level-sets for the three stability regimes

This bulk behaviour suggests that $LAVD$ is indeed capturing structural changes in the organization of the ABL as we transition from a nearly-neutral to a highly unstable atmosphere. One distinct advantage of this approach is the ability to extract the individual material features, and examine the role that each play in land-atmosphere interactions. For computational efficiency in our LES dataset, we extracted coherent Lagrangian vortices as $LAVD$ level-sets, similar to the previous analysis of Aksamit et al. (2023), instead of isolating cylindrical shells surrounding co-dimension two $LAVD$ ridges. Large $LAVD$ values in LES may result from trajectories trapped in rotationally coherent vortices as well as in high shear regions with large vorticity but no apparent vortices. Additionally, there is no standard method for selecting the most appropriate value of an $LAVD$ level-set of interest, though it has been shown that this not of primary importance as any arbitrarily chosen level-set performs as an effective diffusive transport barrier to heat and momentum (Aksamit et al. 2023). We first seek to verify that we can extract influential roll and cell structures via the relaxed $LAVD$ level-set criteria as this not yet known.

To analyze our sixty-minute temporally-resolved LES fields, we implemented a fixed $LAVD$ level-set value for each type of simulation. From figure 4, we see that the near-neutral and transitional cases have the strongest $LAVD$ features immediately above the surface. Additionally, there is not a significant change in mean $LAVD$ across all heights in the convective case. We thus suggest an $LAVD$ level-set value should be chosen to be significantly large relative to values at the lowest height of investigation if one seeks to extract near-surface horizontal rolls. To achieve this for each stability, we used twice the mean $LAVD$ value at 25 metres above the surface (the lower extent of our $LAVD$ analysis) as this allows us to limit our near-neutral analysis to exceptional rolls and while still providing a suitable value to identify convective cells.

In Figure 5 we display $LAVD$ level-sets for the three stabilities calculated in randomly selected ten-second windows. We also compare these structures with the vertical velocity and $LAVD$ fields at the $z = 25\ m$ level. Quasi-linear streamwise organization of features reminiscent of rolls can be clearly seen in Figure 5a for the near-neutral case. There is still some suggestion of linear organization in the transitional case (Figure 5b), but small plumes are also visible throughout the domain. In the unstable atmosphere, features with high $LAVD$ values exhibit no streamwise organization and a much more isotropic distribution of vortices. Generalizing beyond this single realization, we can quantify the mean geometry of vortices in each flow by comparing the orientation of *LAVD* surfaces over the whole sixty-minute periods.

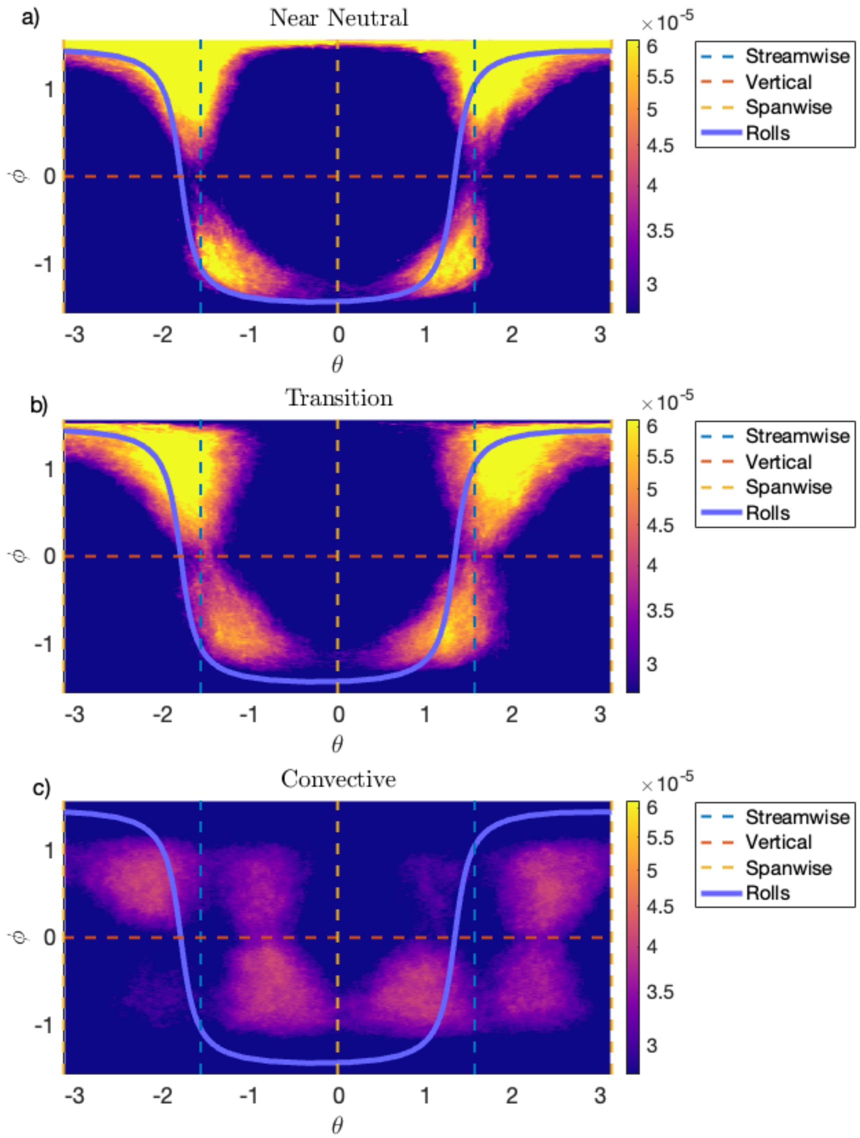


**Fig 6**: Heat map distributions of spherical coordinates of coherent Lagrangian vortex surface normal vectors for the three stability simulations. Distributions are compared to curves that represent streamwise, vertical, and spanwise oriented cylinders, as well as a perfect cylindrical "roll" oriented 15° from streamwise and elevated 30° above the surface

Specifically, for each integration window, we first extract the roll and cell candidates as *LAVD* level-sets at our chosen thresholds, and calculate unit surface normal vectors for a triangulation of the surfaces. By definition, these vectors are aligned with the *LAVD* gradient on each vortical feature. It is widely suggested that horizontal rolls are quasi-linear tube-like features that are oriented between 10° and 30° in the streamwise-spanwise plane away from the streamwise direction (Banghoff et al. 2020), and may be elevated approximately 30° above the surface (Zhou et al. 1999). We use this description as a baseline with which to compare the orientations of our coherent Lagrangian vortices.

By translating each surface unit normal vector to the origin and converting to spherical coordinates, we can compare the distribution of the orientation of surface tangent spaces in the azimuth-elevation plane. With this novel approach, idealized cylindrical vortices will have a distinct signature depending on the direction their rotational axis. We can then compare how closely our vortices approximate these idealized structures.

In Figure 6, we provide heatmap distributions of the fraction of coherent Lagrangian vortex normal vectors for the three stabilities on a $200 \times 200$ grid spanning the azimuth-elevation plane. We also include the theoretical signatures of vertical, spanwise, and streamwise oriented cylinders. We also include the trace of a horizontal cylindrical roll that is rotated away from perfect streamwise alignment. Comparing the three experiments we see that *LAVD* level-sets in near-neutral stability most closely match the idealized roll suggesting not only that PALM is generating the correct structures observed in neutral stability experiments, but that *LAVD* can also be used to extract individual experimentally-verifiable structures in ABL turbulence.

The transitional scenario shows qualitatively similar orientations as the near-neutral rolls, but with a larger degree of scatter. This compliments the findings in Figure 4 that, while the structural organization of turbulence may appear similar, increased convection is modifying the spatial distribution of vortical features as well as their actual shape. Vortices in the convective case shows the widest range of surface-normal orientations, with no distinct alignment with any specific direction. There is an increased probability of normal vector orientations closer to the idealized vertical cylinder than in the near-neutral or transitional cases, but it is not the dominant orientation for the convective case. This suggests a much less linear orientation of cells in convective turbulence, and a more random distribution of cell shapes.

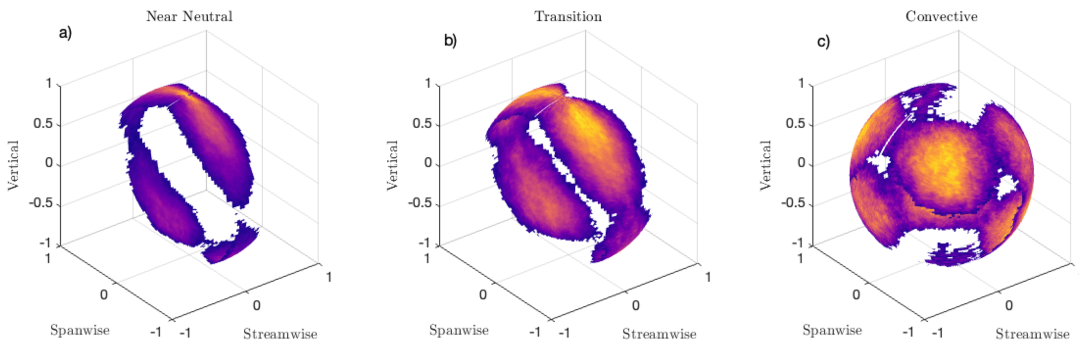


**Fig 7:** Three-dimensional visualization of coherent Lagrangian vortex surface normal vectors distributions in spherical coordinates of for the three stability simulations. Corresponding ABL directions are labeled to interpret the direction that surface normal vectors are typically oriented. The presence of rolls as influential Lagrangian structures is evident in the near neutral and transitional case

In Figure 7 we supplement these heat map distributions by mapping them into spherical coordinates with a fixed radius of one. To aid in visualization, we remove values below a single fixed threshold ($2 \times 10^{-7}\%$) for all three cases. This leaves the approximate orientation of the surface of only the most common vortices. The near-neutral case has the narrowest distribution of surface normal vectors, suggesting we are consistently extracting a recurrent roll structure throughout the whole sixty minutes of simulation. In Figure 6 it is also easier to see the slight elevation angle away from the surface in the near neutral case, though the central axis is closer to 15° than an idealized 30°. As mentioned before, the transitional case has a slightly wider distribution of orientations, though the influence of the roll-structure is still visible. Once we move to the strongly convective case, it is much harder to determine a typical orientation of the surface of a typical vortex, again suggesting a much more isotropic distribution of turbulent coherent structures.

### 3.3 Coherent Lagrangian Vortices and Turbulent Heat Transport

Having shown that *LAVD* level-sets can indeed be used to identify the material boundaries of features that represent experimental descriptions rolls and cells, we now quantify the role of these vortices in the transport of heat in land-atmosphere interactions. We begin by investigating the advective and turbulent transport of heat. As mentioned before, advective and turbulent fluxes vary between different reference frames, and are therefore not representative of inherent physical processes in the wind, but they are nonetheless widely studied in boundary layer meteorology and are useful metrics for comparison and model parameterization. For each simulation, we separate the flow into coherent regions associated with being inside a coherent Lagrangian vortex, and an incoherent region in the surrounding turbulent flow. We then calculate the volume-averaged advective transport of heat ($\overline{w\Theta}$) and volume-averaged vertical turbulent transport of heat ($\overline{w'\Theta'}$) for 60 realizations of *LAVD* fields spanning approximately a 1.5 million cubic metre volume. We also compare the volume-averaged magnitudes of these two fluxes to account for potential cancelations of fluxes of different sign.

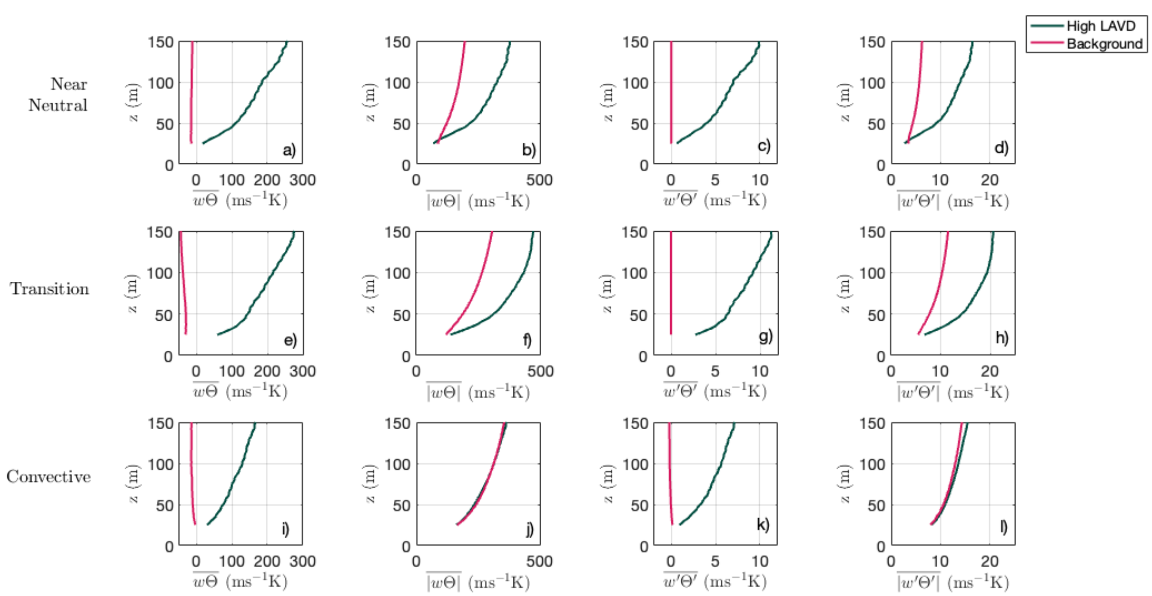


**Fig 8:** Comparison of advective and Turbulent Heat Flux profiles for different stabilities for fluid inside and outside coherent Lagrangian vortices

Figure 8 compares the height-averaged advective and turbulent heat fluxes for the coherent vortex regions and the surrounding incoherent regions of the flow, while Figure 9 shows the ratio of high and low *LAVD* flux values. In low *LAVD* regions, $\overline{w\Theta}$ and $\overline{w'\Theta'}$ are of much smaller magnitude than the high *LAVD* fluid and typically slightly negative. One exception is the near-neutral cases, where $\overline{w'\Theta'}$ in the low *LAVD* region changes sign at approximately 90 metres, as can be clearly seen in Figure 9c. In the near neutral case, mean vertical advective transport of heat inside a coherent Lagrangian vortex is approximately 1.2 times stronger, and in the opposite direction, at z=25 metres, and 20 times stronger at 150 metres. The amplification of advective heat transport is less pronounced for the transitional and convective case, but still ranges from two to twelve times stronger, and away from the surface.

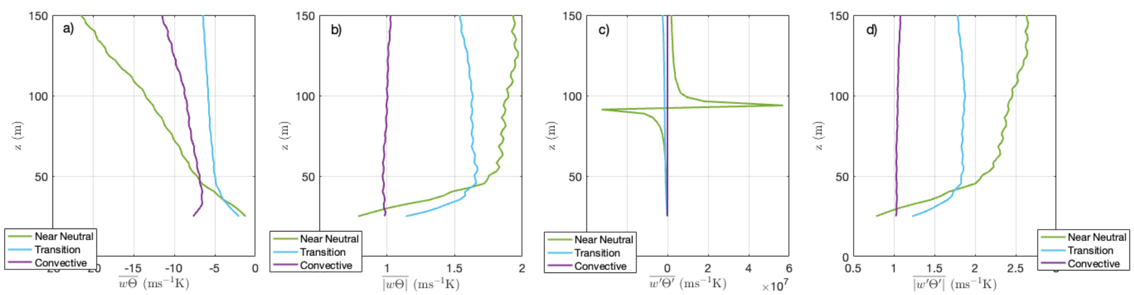


**Fig 9:** Profiles of advective and turbulent heat flux ratios for different stabilities for fluid inside and outside coherent Lagrangian vortices. The values being compared are those in Figure 8

When ignoring the direction of advective heat transport, and compare only the mean magnitudes, we find that coherent Lagrangian vortices, rolls and cell, transport heat much more effectively than the surrounding fluid in the transition and near neutral cases. This is a significant difference, such that preferential sampling in observational studies and accurately resolving a statistically representative number of these structures in modeling studies needs to be considered. For example, a bulk transport coefficient that treats the entire flow domain homogeneously would inaccurately represent the total flux. For the convective case, the ratio of advective magnitudes is much closer to one, signifying a similar ability of coherent vortices and incoherent fluid to transport heat by advection, though only when neglecting the direction of transport.

Volume averages of turbulent fluxes show similar trends, with mean heat flux being of opposite sign, and much larger inside coherent vortices. The magnitude of turbulent heat flux inside vortices also increases with height for all stabilities. Neglecting the sign of turbulent flux, we find a similar trend as in the advective case with near neutral and transitional vortices containing signatures of much larger turbulent fluxes than the incoherent regions, and the coherent and incoherent regions having approximately the same magnitude for the convective case.

### 3.4 Objective Heat and Momentum Transport for roll-cell prediction

As discussed above, turbulent and advective fluxes of heat (and momentum) are frame-dependent diagnostics and insufficient for objectively describing flow physics in thermal fluids. This, and the common assumptions of horizontally homogeneous and flat terrain, makes comparisons of turbulent transport of scalars and momentum between different flow geometries, and their average statistics, highly non-trivial. Furthermore, stability measures based on turbulent fluxes, such as the Obhukhov length, are not robust predictors of the presence rolls or cells in nonstationary flows.

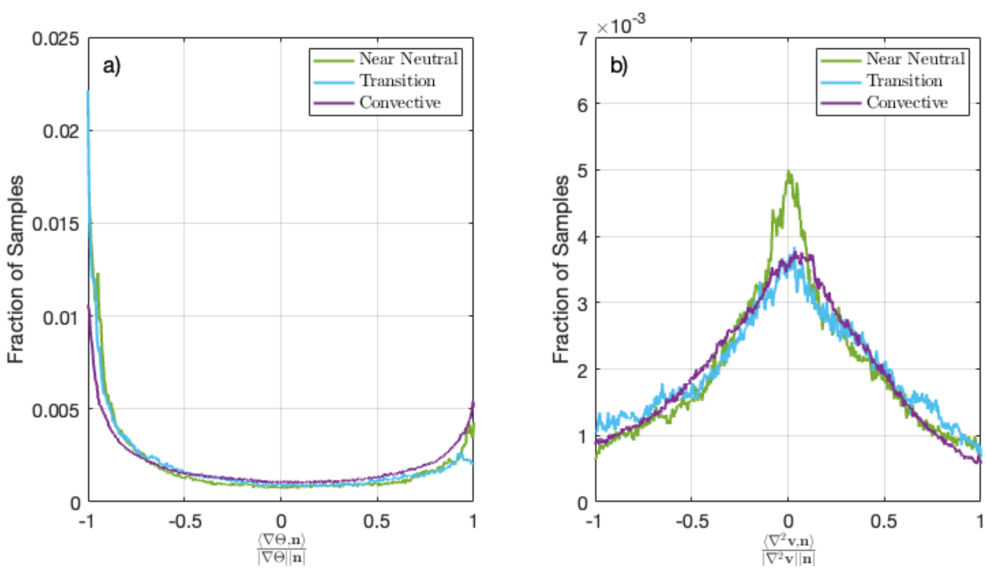


**Fig 10:** Pointwise inner products of normalized diffusive heat flux (panel a) and diffusive momentum flux (panel b) across select LAVD surfaces from Figure 5 for the three stability regimes

Instead of focusing on stability as a prescriptive measure, we now seek to explain the transition from shear-dominated rolls to convective cells by describing the relative influence of objective momentum and heat transport barriers in organizing Lagrangian coherent structures of the flow. Using instantaneous velocity and temperature fields, Aksamit et al. (2023) showed how the alignment of diffusive momentum and heat transport vectors accurately diagnoses the relative influence of Coriolis-enhanced structures and turbulent convective plumes in rotating Rayleigh-Bénard flow. We adapt this theory to differentiate the relative influence of shear and convection generated structures and test it in our ABL simulations. We hypothesize the momentum-heat barrier findings from Aksamit et al. (2023) may be adapted as follows.

In the near-neutral atmosphere, weak temperature gradients do not result in the creation of convective cells, and thus air temperature behaves more like a passive scalar that is organized by Lagrangian coherent structures. Large temperature gradients are generated across surfaces of distinct LCS, and thus LCS are closely aligned with diffusive transport maximizers in the flow. At the same time, momentum plays a significant role in organizing LCSs when convective influences are weak, with diffusive momentum transport barriers closely aligned with Lagrangian coherent structures, and momentum being convected along with the LCSs. In this scenario, gradients of temperature would be orthogonal to the Laplacian of the velocity field as the former is the direction of diffusive heat flux and the latter represents diffusive momentum flux.

As the relative influence of shear decreases and convection increases, momentum and heat both compete to modify the velocity field, which in turn modifies the distribution of momentum and heat. As was seen with the decreased influence of the Coriolis force in rotating Rayleigh-Bénard convection, homogeneous regions of heat may become less aligned with momentum when convection becomes more influential (Aksamit et al. 2023). This results in a loss of momentum and heat transport barrier alignment, and a decreased orthogonality of diffusive heat and momentum fluxes.

In Figure 10, we start with an individual example and evaluate the inner product of heat and momentum flux vectors ($\nabla\Theta$ and $\Delta v$, respectively) with surface normal vectors on the $LAVD$ level-sets isolated in Figure 5. Figure 10a shows a high degree of alignment between vortex surface normal vectors and diffusive heat flux, suggesting the vortices are effectively constraining the distribution of heat by maximizing the temperature gradient across their borders. The orthogonality of $LAVD$ level-set surfaces and the diffusive heat flux decreases with decreasing stability, suggesting a decreased ability to perfectly resolve heat transport barriers by *LAVD* alone. As mentioned before, *LAVD* was mathematically derived to identify rotationally coherent vortices, and is independent of heat transport. Other Lagrangian diagnostics that minimize and maximize diffusive flux (i.e., diffusion barrier strength, (Haller et al. 2018)) are better suited for this purpose.

In Figure 10b, we compare the ability of our rolls and cells to block the objective transport of momentum across their surface. Vortices in near neutral condition have the greatest degree of tangency, but it is notable that tangency for the transitional and convective cases is comparable. This contrasts with the heat-blocking abilities of these same surfaces that actually decreases from the transitional to convective scenario. It is encouraging to see how even a rough numerical approximation of objective and material structures with *LAVD* level-sets can both extract rolls and cells, as well as provide physically meaningful comparisons of momentum and heat flux through those surfaces.

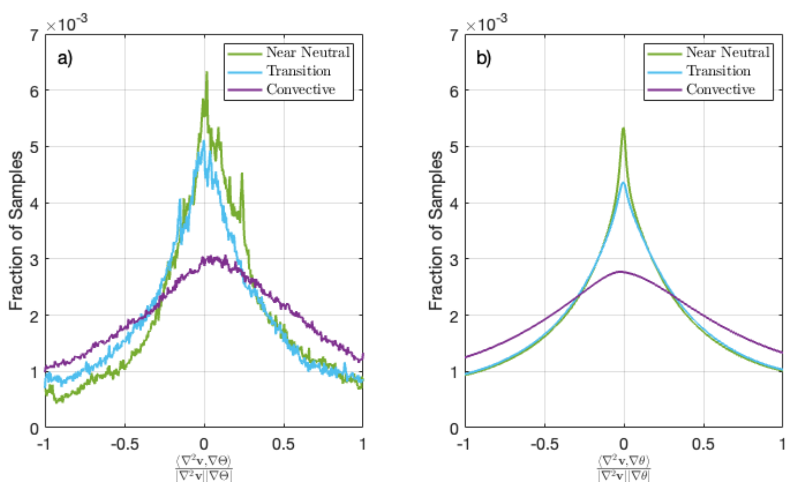


**Fig 11:** Pointwise inner products of normalized diffusive momentum and heat transport vector fields for the three stability regimes. In panel a) we show the selected inner products on the specific LAVD surfaces from Figure 5. Panel b) displays the bulk inner products for the entire simulations. Orthogonality increases as shear-driven structures (rolls) exhibit outsized control on the organization of heat distributions

The ability of coherent Lagrangian vortices to block momentum and heat transport varies as we change stability, but we can also investigate the alignment of momentum and heat barriers themselves in each flow. In Figure 11a we show how momentum and heat flux vectors align with each other on the same *LAVD* features examined in Figures 5 and

10. We find the strongest agreement on vortices in the near-neutral and transition cases, with decreasing alignment as we increase convection. Generalizing to the entire flow, we also calculate inner products of heat and momentum flux vectors for all the datapoints resolved in our large eddy simulations. Figure 11b clearly shows a decreasing alignment of heat and momentum transport with increasing convection, but all three stabilities have a clear orthogonality preference, even when considering vectors not on the surface of coherent Lagrangian vortices. This suggests a general agreement of heat and momentum transport pathways, but that the transport of heat and momentum varies more as convective cells begin to generate their own momentum, and alter the structure of momentum barriers.

# 4 Conclusions and Outlook

The transition from horizontal rolls to convective cells is a complex turbulence organization problem resulting from competing physical influences that are poorly understood. To study the behaviour of the atmospheric boundary layer under varying stabilities, we introduced several new computational tools that identify atmospheric structures as frame-indifferent and material features that exhibit exceptional rotation and temporal coherence. The frame-indifference of our approach allows a physically meaningful comparison with experimentally-observed tracer-organizing structures. This contrasts with previous numerical investigations into ABL structure which rely on statistical descriptions or correlations with frame-dependent diagnostic fields, and do not actually extract temporally coherent fluid surfaces.

Being the first study to identify rolls and cells as *LAVD* level-sets, we compared several geometric quantities of our surfaces with classic descriptions from experimental observations. Two novel structure orientation visualization techniques allowed deeper insight into the bulk geometry of coherent Lagrangian vortices for each stability, and opens the door for future comparisons with other studies. We also qualitatively verified that the individual *LAVD* structures we extracted do represent rolls and cells in the existing literature.

We found that rolls and cells play an outsized role for turbulent and convective heat fluxes when compared with other turbulent motions. In the near-neutral and transitional atmosphere, high *LAVD* regions showed significant amplification of these spatially averaged fluxes, and their spatially averaged magnitudes, when compared with the surrounding fluid. For the convective atmosphere, the magnitude of convective and turbulent fluxes was more evenly distributed inside and outside coherent Lagrangian vortices, but total fluxes were still significantly larger. This suggests that the strength of turbulence may be more isotropically distributed inside and outside rotational features in the unstable boundary layer, but convective cells play a specific role in directing turbulent and convective fluxes.

Finally, we utilized recent developments in the theory of diffusive momentum and heat transport to describe the roles of shear and convective forces in a manner that is objective, spatially and temporally resolved, and makes no assumptions on the geometry or structure of the flow. The relative alignment of momentum and heat transport barriers was found to correspond with the presence of horizontal rolls or convective cells. This extends previous work that draws connections between mechanical and thermal influences with the type of structures present in rotating Rayleigh-Bénard flow by way of momentum and heat transport.

The relationship we found between objectively-defined momentum and heat transport with the roll-cell transition suggests a physics-based understanding of this process may be possible. The dominant influence of momentum barriers in the near-neutral atmosphere, and complex the heat-momentum feedback in the unstable atmosphere provides an intuitive description of this transition from physically meaningful vector fields.

By approaching the study of rolls and cells as objective and material structures, and studying momentum and heat transport through objective flux definitions, we do not rely on a given orientation or statistical stationarity to identify relevant fluid features. This may not be of primary concern to boundary layer meteorologists that analyze time series data from meteorological towers. However, when describing physical turbulent phenomena in both spatially resolved numerical simulations and field observations, it is important to consider whether or not diagnostics are meaningful in both scenarios, and if there are fundamental benchmarks that are met in one (e.g., frame-indifference for structure identification) we should at the very least consider this when attempting to discover common ground.

Frame-indifferent descriptions of structures and fluxes also removes the need of many common assumptions for comparing the transport of scalars in ABLs, such as horizontally homogeneous terrain. In this way, our research is a proof-of-concept for a benchmark methodology that is suitable for comparing the existence and importance of atmospheric structures between flows in complex terrain, unsteady and transitional flows, flows around objects, and many otherwise incomparable situations.

# 5 Appendix

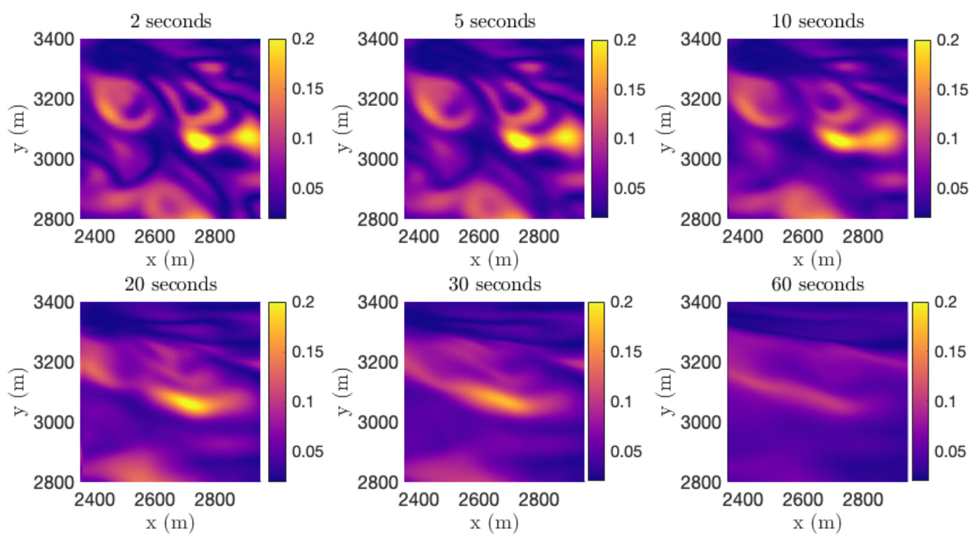


**Fig 12:** Effect of increasing integration time for LAVD fields at z=25 m. For 2 to 20 seconds, the dominant rotating structures appear in the same locations, but longer integration times reduce their impact on fluid trajectories as the material rotation is averaged over longer distances

In this appendix we provide a simple qualitative comparison of *LAVD* fields in the near-neutral boundary layer as calculated on the z=25 m plane. We compare advection times spanning two seconds to 60 seconds in Figure 12. At longer advection times, fluid particles interact with multiple turbulent coherent flow features, and *LAVD* fields are no longer representative of structures adjacent to initial fluid particle positions at the beginning of advection where the *LAVD* values are mapped. From two to ten seconds, there are only minor differences in *LAVD* fields, while at twenty seconds turbulent motions already begin to obscure and elongate features. Beyond twenty seconds, full detail of the coherent fluid behaviour at the spatial scales resolved in Figure 12 is largely lost.

## References


Abernathey R, Haller G (2018) Transport by Lagrangian vortices in the eastern Pacific. J Phys Oceanogr 48:667–685. https://doi.org/10.1175/JPO-D-17-0102.1

Adrian RJ, Meinhart CD, Tomkins CD (2000) Vortex organization in the outer region of the turbulent boundary layer. J Fluid Mech 422:1–54. https://doi.org/10.1017/S0022112000001580

Aksamit NO, Haller G (2022) Objective momentum barriers in wall turbulence. J Fluid Mech 941:1–35. https://doi.org/10.1017/jfm.2022.316

Aksamit NO, Hartmann R, Lohse D, Haller G (2023) Interplay between advective, diffusive, and active barriers in Rayleigh-Bénard flow. J Fluid Mech 969:A27. https://doi.org/10.1017/jfm.2023.563

Aksamit NO, Kravitz B, Macmartin DG, Haller G (2021) Harnessing Stratospheric Diffusion Barriers for Enhanced Climate Geoengineering. Atmos Chem Phys 21:8845–8861. https://doi.org/doi.org:10.5194/acp-21-8845-2021

Astarita G (1979) Objective and generally applicable criteria for flow classification. J Nonnewton Fluid Mech 6:69–76. https://doi.org/10.1016/0377-0257(79)87004-4

Banghoff JR, Sorber JD, Stensrud DJ, et al (2020) A 10-year warm-season climatology of horizontal convective rolls and cellular convection in Central Oklahoma. Mon Weather Rev 148:21–42. https://doi.org/10.1175/MWR-D-19-0136.1

Beron-Vera FJ, Hadjighasem A, Xia Q, et al (2019) Coherent Lagrangian swirls among submesoscale motions. Proc Natl Acad Sci U S A 116:18251–18256. https://doi.org/10.1073/pnas.1701392115

Beron-Vera FJ, Olascoaga MJ, Brown MG, Koçak H (2012) Zonal jets as meridional transport barriers in the subtropical and polar lower stratosphere. J Atmos Sci 69:753–767. https://doi.org/10.1175/JAS-D-11-084.1

BozorgMagham AE, Ross SD (2015) Atmospheric Lagrangian coherent structures considering unresolved turbulence and forecast uncertainty. Commun Nonlinear Sci Numer Simul 22:964–979. https://doi.org/10.1016/j.cnsns.2014.07.011

Christian TW, Wakimoto RM (1989) The Relationship between Radar Reflectivities and Clouds Associated with Horizontal Roll Convection on 8 August 1982. Mon Weather Rev 117:1530–1544

Deardorff JW (1972) Numerical Investigation of Neutral and Unstable Planetary Boundary Layers. J Atmos Sci 29:91–115

Dong Y, Tian W (2020) On the thresholds of vortex visualisation methods. Int J Comut Fluid Dyn 34:267–277. https://doi.org/10.1080/10618562.2020.1745781

Drouot R (1976) Definition d’un transport associe un modele de fluide de deuxieme ordre. C R Acad Sci Pari Ser A 282:923–926

Drouot R, Lucius M (1976) Approximation du second ordre de la loi de comportement des fluides simples. Lois classiques deduites de l’introduction d’un nouveau tenseur objectif. Arch Mech Stos 28:189=198

Eisma J, Westerweel J, van de Water W (2021) Do coherent structures organize scalar mixing in a turbulent boundary layer? J Fluid Mech 929:1–19. https://doi.org/10.1017/jfm.2021.821

Foken T (2008) Micrometeorology. Springer, Berlin

Foken T, Aubinet M, Finnigan JJ, et al (2011) Results of a panel discussion about the energy balance closure correction for trace gases. Bull Am Meteorol Soc 92:13–18. https://doi.org/10.1175/2011BAMS3130.1

Gao Q, Ortiz-Dueñs C, Longmire EK (2011) Analysis of vortex populations in turbulent wall-bounded flows. J Fluid Mech 678:87–123. https://doi.org/10.1017/jfm.2011.101

Garaboa-Paz D, Eiras-Barca J, Huhn F, Peérez-Mũnuzuri V (2015) Lagrangian coherent structures along atmospheric rivers. Chaos 25:. https://doi.org/10.1063/1.4919768

Green MA, Rowley CW, Haller G (2007) Detection of Lagrangian coherent structures in three-dimensional turbulence. J Fluid Mech 572:111–120. https://doi.org/10.1017/S0022112006003648

Grossman RL (1982) An analysis of vertical velocity spectra obtained in the bomex fair-weather, trade-wind boundary layer. Boundary Layer Meteorol 23:323–357. https://doi.org/10.1007/BF00121120

Günther T, Horváth Á, Bresky W, et al (2021) Lagrangian Coherent Structures and Vortex Formation in High Spatiotemporal-Resolution Satellite Winds of an Atmospheric Kármán Vortex Street. Journal of Geophysical Research: Atmospheres 126:1–23. https://doi.org/10.1029/2021JD035000

Gurtin ME (1981) An Introduction to Continuum Mechanics, 1st edn. Academic Press, San Diego, USA

Haller G (2020) Can vortex criteria be objectivized? J Fluid Mech 908:. https://doi.org/10.1017/jfm.2020.937

Haller G (2005) An objective definition of a vortex. J Fluid Mech 525:1–26. https://doi.org/10.1017/S0022112004002526

Haller G (2023) Transport Barriers in Flow Data: Advective, Diffusive, Stochastic and Active Methods. In: Transport Barriers and Coherent Structures in Flow Data. Cambridge University Press, Cambridge, UK

Haller G, Hadjighasem A, Farazmand M, Huhn F (2016) Defining coherent vortices objectively from the vorticity. J Fluid Mech 795:136–173. https://doi.org/10.1017/jfm.2016.151

Haller G, Karrasch D, Kogelbauer F (2018) Material barriers to diffusive and stochastic transport. Proceedings of the National Academy of Sciences 115:9074–9079. https://doi.org/10.1073/pnas.1720177115

Haller G, Katsanoulis S, Holzner M, et al (2020) Objective barriers to the transport of dynamically active vector fields. J Fluid Mech 905:. https://doi.org/10.1017/jfm.2020.737

He GS, Pan C, Feng LH, et al (2016) Evolution of Lagrangian coherent structures in a cylinder-wake disturbed flat plate boundary layer. J Fluid Mech 792:274–306. https://doi.org/10.1017/jfm.2016.81

Hunt JCR, Wray a a, Moin P (1988) Eddies, streams, and convergence zones in turbulent flows. Center for Turbulence Research, Proceedings of the Summer Program 193–208. https://doi.org/CTR-S88

Jayaraman B, Brasseur JG (2021) Transition in atmospheric boundary layer turbulence structure from neutral to convective, and large-scale rolls. J Fluid Mech 913:1–31. https://doi.org/10.1017/jfm.2021.3

Jeong J, Hussain F (1995) On the Identification of a vortex. Jounral of Fluid Mechanics 285:69–94. https://doi.org/10.1109/TCT.1956.1086328

Kaszás B, Pedergnana T, Haller G (2023) The objective deformation component of a velocity field. European Journal of Mechanics, B/Fluids 98:211–223. https://doi.org/10.1016/j.euromechflu.2022.12.007

Khanna S, Brasseur JG (1998) Three-dimensional buoyancy- and shear-induced local structure of the atmospheric boundary layer. J Atmos Sci 55:710–743. https://doi.org/10.1175/1520-0469(1998)055<0710:TDBASI>2.0.CO;2

Kline S, Reynolds W, Schraub F, Runstadler P (1967) The structure of turbulent boundary layers. J Fluid Mech 30:741–773

Knutson B, Tang W, Chan PW (2015) Lagrangian coherent structure analysis of terminal winds: Three-dimensionality, intramodel variations, and flight analyses. Advances in Meteorology 2015:. https://doi.org/10.1155/2015/816727

Lehner M, Rotach MW (2018) Current challenges in understanding and predicting transport and exchange in the atmosphere over mountainous terrain. Atmosphere (Basel) 9:. https://doi.org/10.3390/atmos9070276

LeMone MA (1976) Modulation of Turbulence Energy by Longitudinal Rolls in an Unstable Planetary Boundary Layer. J Atmos Sci 33:1308–1320

LeMone MA (1973) The Structure and Dynamics of Horizontal Roll Vortices in the Planetary Boundary Layer. J Atmos Sci 30:1077–1091

Liu J, Gao Y, Liu C (2019a) An objective version of the Rortex vector for vortex identification. Physics of Fluids 31:. https://doi.org/10.1063/1.5095624

Liu J, Gao Y sheng, Wang Y qian, Liu C (2019b) Objective Omega vortex identification method. Journal of Hydrodynamics 31:455–463. https://doi.org/10.1007/s42241-019-0028-y

Lu SS, Willmarth WW (1973) Measurements of the structure of Reynolds stress in a turbulent boundary layer. J Fluid Mech 60:481–511

Lugt HJ (1979) The Dilemma of Defining a Vortex. In: Müller U., Roesner K.G. SB (ed) Recent Developments in Theoretical and Experimental Fluid Mechanics. Springer, Berlin, Heidelberg

Maronga B, Banzhaf S, Burmeister C, et al (2020) Overview of the PALM model system 6.0

Mauder M, Foken T, Cuxart J (2020) Surface-Energy-Balance Closure over Land: A Review. Springer Netherlands

Moeng C-H, Sullivan PP (1994) A Comparison of Shear and Buoyancy-Driven Planetary Boundary Layer Flows. J Atmos Sci 51:999–1022

Neamtu-Halic MM, Krug D, Haller G, Holzner M (2019) Lagrangian coherent structures and entrainment near the turbulent/non-Turbulent interface of a gravity current. J Fluid Mech 877:824–843. https://doi.org/10.1017/jfm.2019.635

Olascoaga MJ, Brown MG, Beron-Vera FJ, Koçak H (2012) Stratospheric winds, transport barriers and the 2011 Arctic ozone hole. Nonlinear Process Geophys 19:687–692. https://doi.org/10.5194/npg-19-687-2012

Pan C, Wang JJ, Zhang C (2009) Identification of lagrangian coherent structures in the turbulent boundary layer. Science in China, Series G: Physics, Mechanics and Astronomy 52:248–257. https://doi.org/10.1007/s11433-009-0033-1

Park SB, Baik JJ (2014) Large-eddy simulations of convective boundary layers over flat and urbanlike surfaces. J Atmos Sci 71:1880–1892. https://doi.org/10.1175/JAS-D-13-0191.1

Peacock T, Haller G (2013) Lagrangian coherent structures: The hidden skeleton of fluid flows. Phys Today 66:41–47. https://doi.org/10.1063/PT.3.1886

Rutherford B, Dangelmayr G, Montgomery MT (2012) Lagrangian coherent structures in tropical cyclone intensification. Atmos Chem Phys 12:5483–5507. https://doi.org/10.5194/acp-12-5483-2012

Salesky ST, Chamecki M, Bou-Zeid E (2017) On the Nature of the Transition Between Roll and Cellular Organization in the Convective Boundary Layer. Boundary Layer Meteorol 163:41–68. https://doi.org/10.1007/s10546-016-0220-3

Schalkwijk J, Jonker HJJ, Siebesma AP, Van Meijgaard E (2015) Weather forecasting using GPU-based large-Eddy simulations. Bull Am Meteorol Soc 96:715–723. https://doi.org/10.1175/BAMS-D-14-00114.1

Serafin S, Adler B, Cuxart J, et al (2018) Exchange Processes in the Atmospheric Boundary Layer Over Mountainous Terrain. Atmosphere (Basel) 9:102. https://doi.org/10.3390/atmos9030102

Serra M, Sathe P, Beron-Vera F, Haller G (2017) Uncovering the edge of the polar vortex. J Atmos Sci 74:3871–3885. https://doi.org/10.1175/JAS-D-17-0052.1

Speziale CG (1998) A review of material frame-indifference in mechanics. Appl Mech Rev 51:489–504. https://doi.org/10.1115/1.3099017

Speziale CG (1979) Invariance of turbulent closure models. Physics of Fluids 22:1033–1037. https://doi.org/10.1063/1.862708

Svensson N, Sahlée E, Bergström H, et al (2017) A Case Study of Offshore Advection of Boundary Layer Rolls over a Stably Stratified Sea Surface. Advances in Meteorology 2017:. https://doi.org/10.1155/2017/9015891

Tallapragada P, Ross SD, Schmale DG (2011) Lagrangian coherent structures are associated with fluctuations in airborne microbial populations. Chaos 21:. https://doi.org/10.1063/1.3624930

Tang W, Chan PW, Haller G (2011) Lagrangian coherent structure analysis of terminal winds detected by lidar. Part I: Turbulence structures. J Appl Meteorol Climatol 50:325–338. https://doi.org/10.1175/2010JAMC2508.1

Truesdell C, Noll W (2004) The Non-Linear Field Theories of Mechanics, 3rd edn. Springer

Wallace JM (2016) Quadrant Analysis in Turbulence Research: History and Evolution. Annu Rev Fluid Mech 48:131–158. https://doi.org/10.1146/annurev-fluid-122414-034550

Wang N, Ramirez U, Flores F, Datta-Barua S (2017) Lagrangian coherent structures in the thermosphere: Predictive transport barriers. Geophys Res Lett 44:4549–4557. https://doi.org/10.1002/2017GL072568

Weckwerth TM, Horst TW, Wilson JW (1999) An observational study of the evolution of horizontal convective rolls. Mon Weather Rev 127:2160–2179. https://doi.org/10.1175/1520-0493(1999)127<2160:AOSOTE>2.0.CO;2

Weckwerth TM, Wilson JW, Wakimoto RM, Crook NA (1997) Horizontal convective rolls: Determining the environmental conditions supporting their existence and characteristics. Mon Weather Rev 125:505–526. https://doi.org/10.1175/1520-0493(1997)125<0505:HCRDTE>2.0.CO;2

Westerweel J, Fukushima C, Pedersen JM, Hunt JCR (2009) Momentum and scalar transport at the turbulent/non-turbulent interface of a jet. J Fluid Mech 631:199–230. https://doi.org/10.1017/S0022112009006600

Wilson ZD, Tutkun M, Cal RB (2013) Identification of Lagrangian coherent structures in a turbulent boundary layer. J Fluid Mech 728:396–416. https://doi.org/10.1017/jfm.2013.214

Yagi A, Inagaki A, Kanda M, et al (2017) Nature of Streaky Structures Observed with a Doppler Lidar. Boundary Layer Meteorol 163:19–40. https://doi.org/10.1007/s10546-016-0213-2

Young G, Kristovich D, Hjelmfelt M, Foster R (2002) Rolls, streets, waves, and more: A review of quasi-two-dimensional structures in the atmospheric boundary layer. Bull Am Meteorol Soc 997–1001

Zhou J, Adrian RJ, Balachandar S, Kendall TM (1999) Mechanisms for generating coherent packets of hairpin vortices in channel flow. J Fluid Mech 387:353–396. https://doi.org/10.1017/S002211209900467X